EDGE ARTICLE

Check for updates

Guest induced reversible on–off switching of elastic frustration in a 3D spin crossover coordination polymer with room temperature hysteretic behaviour†

Lucía Piñeiro-López,‡[a] Francisco-Javier Valverde-Muñoz, ‡[a] Elzbieta Trzop,[b] M. Carmen Muñoz, [c] Maksym Seredyuk, [ad] Javier Castells-Gil, [a] Iván da Silva, [e] Carlos Martí-Gastaldo, [a] Eric Collet *[b] and José Antonio Real *[a]

A binary reversible switch between low-temperature multi-step spin crossover (SCO), through the evolution of the population $\gamma_{HS}(T)$ with high-spin (HS)-low-spin (LS) sequence: HS_1LS_0 (state 1) $\leftrightarrow$ $HS_{2/3}LS_{1/3}$ (state 2) $\leftrightarrow$ $HS_{1/2}LS_{1/2}$ (state 3) $\leftrightarrow$ $HS_{1/3}LS_{2/3}$ (state 4) $\leftrightarrow$ HS_0LS_1 (state 5), and complete one step hysteretic spin transition featuring 20 K wide thermal hysteresis centred at 290 K occurs in the three-dimensional (3D) Hofmann-type porous coordination polymer {Fe^{II}(3,8phen)[Au(CN)$_2$]$_2$}·xPhNO$_2$ (3,8phen = 3,8-phenanthroline, PhNO$_2$ = nitrobenzene), made up of two identical interpenetrated pcu-type frameworks. The included PhNO$_2$ guest ($x = 1$, **1**·**PhNO$_2$**) acts as a molecular wedge between the interpenetrated 3D frameworks *via* PhNO$_2$-3,8phen intermolecular recognition and is the source of the strong elastic frustration responsible for the multi-step regime. Detailed X-ray single crystal analysis reflects competition between spatial periodicities of structurally inequivalent HS and LS SCO centres featuring: (i) symmetry breaking (state 3) with ···HS–LS··· ordering with $\gamma_{HS} = 1/2$; and (ii) occurrence of spatial modulation of the structure providing evidence for stabilization of local or aperiodic ordered mixed spin states for states 2 and 4 (with $\gamma_{HS} \approx 2/3$) and 4 (with $\gamma_{HS} \approx 1/3$), respectively. Below *c.a.* 20 K, structural and magnetic analyses show the photogeneration of a metastable HS*, state 6. The room-temperature single-step hysteretic regime appears with release of the guest ($x = 0$, **1**) and the elastic frustration, and reversibly switches back to the original four-step behaviour upon guest re-adsorption. Both uncommon relevant SCO events meeting in the same material represent a rare opportunity to compare them in the frame of antiferro- and ferro-elastic transitions.

[a]Departamento de Química Inorgánica, Instituto de Ciencia Molecular (ICMol), Universidad de Valencia, Valencia, Spain. E-mail: jose.a.real@uv.es

[b]Univ Rennes, CNRS, IPR (Institut de Physique de Rennes) - UMR 6251, F-35000 Rennes, France. E-mail: eric.collet@univ-rennes1.fr

[c]Departamento de Física Aplicada, Universitat Politècnica de València, Camino de Vera s/n, E-46022, Valencia, Spain

[d]Department of Chemistry, Taras Shevchenko National University of Kyiv, 64/13, Volodymyrska Street, 01601, Kyiv, Ukraine

[e]ISIS Neutron Facility, STFC Rutherford Appleton Laboratory, Chilton, Oxfordshire OX11 0QX, UK

‡ These authors contributed equally to this work.

Introduction

Fe^{II} spin crossover (SCO) complexes are relevant switchable molecular materials that reversibly change between the high-spin (HS, $t_{2g}^4 e_g^2$, $S = 2$) and low-spin (LS, $t_{2g}^6 e_g^0$, $S = 0$) states by the action of a variety of external stimuli (temperature, pressure, light irradiation or analytes) inducing significant changes in the materials' magnetic, electrical and optical properties. Furthermore, due to the antibonding nature of the e$_g$ orbitals, their population–depopulation upon the HS $\leftrightarrow$ LS switch is strongly coupled with structural changes primarily affecting the [Fe^{II}N$_6$] coordination sphere and spreading cooperatively from one SCO centre to another across the crystal through intermolecular contacts (π-stacking and hydrogen bonding) and/or covalent and coordination bonds.[1] Thus, the thermal dependence of the HS (LS) population, $\gamma_{HS}(T)$, is critically affected by the elastic coupling between the active SCO centres, which is usually assumed to be of purely elastic nature.[2–4]

It has been recently shown that the occurrence of competing elastic interactions in the crystal, *i.e.* elastic frustration,[4–6] is pivotal in the rationalization of most relevant experimentally observed $\gamma_{HS}(T)$ dependences. The lack of significant elastic frustration combined with strong coupling favours highly cooperative bistable hysteretic single-step SCO behaviour conferring a binary on–off nature to the electronic and mechanical properties of the material. In contrast, above a certain threshold elastic frustration, $\gamma_{HS}(T)$ reveals the emergence of an intriguing multistep behaviour. At microscopic level, the steps reflect long-range ordering sequences of HS and LS sites, initially symmetry equivalent, and forming spin-state concentration waves. It results from the competition between local "anti-ferro" elastic interactions, minimizing the elastic energy cost through the alternation of sites of different HS and LS states of high and low volumes, and long-range "ferro" elastic interactions, as a macroscopic volume change will favour the same spin state.[4] Both, multistability and room temperature hysteresis are rare events that have raised substantial expectations on the conception of bistable and multiple-bit SCO-based sensors, actuators and memories.[7]

The control of the coupling between the SCO centres for the design of materials with targeted SCO properties is challenging due to the elusive nature of the intermolecular interactions involved and the extreme sensitivity of the SCO phenomenon to minute structural changes. However, the polymeric approach has revealed to be an important tool to test the coupling between the active centres and its effect on the SCO behaviour. This approach has mitigated in part the dominance of the supramolecular interactions characteristic of discrete SCO compounds by replacing these soft interactions with more controllable covalent and coordination bonds. In this respect, Hofmann-type cyanometallate coordination polymers (CPs) $\{Fe^{II}(L)_n[M^{II}(CN)_4]\}$ (M^{II} = Ni, Pd, Pt) have become excellent testbeds for analysing the coupling between the octahedral SCO $[Fe^{II}N_6]$ nodes,[8] which are equatorially connected by 4 cyanometallate bridging groups defining robust square grid layers $\{Fe^{II}_2[M^{II}(CN)_4]_2\}_\infty$. The remaining axial positions are filled with pyridine-like monodentate ($n = 2$) or bis-monodentate ($n = 1$) bridging ligands affording 2D and/or 3D CPs, respectively. For 2D CPs, constructive elastic interactions between consecutive layers can be achieved by π-interactions thanks to the interdigitation of the axial ligands. This is clearly illustrated for the derivatives with L = 3-Xpyridine (X = F,[9] NH$_2$;[10] M^{II} = Ni, Pd, Pt) and triazole-based ligands thiome[11] and proptrz.[12] Similar efficient coupling is achieved when connecting the layers through rigid pyrazine ligands to generate 3D porous fsc-type frameworks (M^{II} = Ni, Pd, Pt).[13] All these CPs display strong cooperative single-step SCO featuring wide hysteretic behaviour at relatively high temperatures. Comparable efficiency has also been observed for the Hofmann variant $\{Fe^{II}(L)[Au^I(CN)_2]_2\}$, a 3D system made up of $\{Fe^{II}_4[Au^I(CN)_2]_4\}_\infty$ grids pillared by L = pyrazine (pz)[14] or fluoropyrazine (Fpz)[15] defining double interpenetrated pcu-type frameworks. However, this efficient communication and synchronization between the active Fe^{II} SCO centres may be modulated or even disrupted by the inclusion of guest molecules since they may act as sources of

elastic frustration and multistability. For example, spin-state concentration waves may form at $\gamma_{HS} \approx 1 \leftrightarrow 1/2 \leftrightarrow 1/3 \leftrightarrow 0$ as it has been described for the 3D SCO-CP $[Fe^{II}(dpsme)Pt(CN)_4] \cdot 2/3dpsme \cdot xEtOH \cdot yH_2O$ and $[Fe^{II}(Phtrz)_2\{Pd(CN)_4\}] \cdot 2H_2O$ where dpsme is the non-rigid bridging ligand 4,4′-di(pyridylthio)methane[16] and Phtrz = (E)-1-phenyl-N-(1,2,4-triazole-4-yl)-methanimine).[17] More recently, a four step SCO behaviour has been described for the 2D CPs $[Fe^{II}(saltrz)_2\{M(CN)_4\}] \cdot 8/3H_2O$ (saltrz = (E)-2-(((4H-1,2,4-triazol-4-yl)imino)methyl)phenol, M = Pt^{II}, Pd^{II})[18] showing steps between plateaus at $\gamma_{HS} \approx 1 \leftrightarrow 5/6 \leftrightarrow 4/6 \leftrightarrow 1/6 \leftrightarrow 0$. Similarly, four steps have been described for the 3D CPs $[Fe^{II}(bipydz)\{Au(CN)_2\}_2] \cdot 4EtOH$ (bipydz = 3,6-bis(4-pyridyl)-1,2-diazine)[19] and $[Fe^{II}(4-abpt)\{Ag(CN)_2\}_2] \cdot 2DMF \cdot EtOH$ (4-abpt = 4-amino-3,5-bis(4-pyridyl)-1,2,4-triazole)[20] with sequences $\gamma_{HS} = 1 \leftrightarrow 2/3 \leftrightarrow 1/2 \leftrightarrow 1/3 \leftrightarrow 0$ and $1 \leftrightarrow 3/4 \leftrightarrow 1/2 \leftrightarrow 1/4 \leftrightarrow 0$, respectively.

Here we report the synthesis and characterization of an unprecedented dual Hofmann-type SCO-CP formulated $\{Fe^{II}(3,8-phen)[Au(CN)_2]_2\} \cdot xPhNO_2$ ($1 \cdot xPhNO_2$) with low dielectric constant pores capable of discriminating between hydroxylic solvents (*i.e.* methanol) and benzene derivatives (*i.e.* PhNO$_2$). The system reversibly switches between a multi-step SCO regime with sequence $\gamma_{HS} = 1 \leftrightarrow \sim2/3 \leftrightarrow 1/2 \leftrightarrow \sim1/3 \leftrightarrow 0$ for $x = 1$ ($1 \cdot PhNO_2$) and a complete single step hysteretic spin transition upon guest removal, $x = 0$ (1), featuring a *c.a.* 20 K wide thermal hysteresis centred at room temperature (290 K). The state 3 at $\gamma_{HS} = 1/2$ features symmetry breaking with an ordered $\cdots$LS–HS$\cdots$ sequence, forming a spin state concentration wave.

The states 2 and 4 around $\gamma_{HS} \approx 1/3$ and $2/3$ are associated with aperiodic structural modulations. The modulation of the Fe–N bonds found for state 4 reveals the spatial modulation of γ_{HS}.

Preparation

Crystalline samples of $1 \cdot PhNO_2$ were grown by slow liquid–liquid diffusion technique using a modified H-vessel with a third tube added due to the poor solubility of the 3,8-phen ligand in methanol. The peripheral tubes contained Fe(BF$_4$)$_2$·6H$_2$O and K[Au(CN)$_2$] salts, respectively while the central tube contained 3,8-phen ligand (see ESI for more information†). Each tube was partially filled with methanol and then with a solution 1 : 10 of PhNO$_2$ in methanol, finally the tubes were sealed. Yellow cube-shaped single crystals were formed two weeks later in the tube which originally contained Fe(BF$_4$)$_2$·6H$_2$O salt with relative high yield (*ca.* 50%). The presence and quantification of the guest molecule was confirmed by means of single-crystal X-ray diffraction, IR spectroscopy (Fig. S1†), thermogravimetric (Fig. S2†) and elemental analysis. Firmly fastened, the guest PhNO$_2$ molecule desorbs in two consecutive steps centred at *ca.* 410 and 470 K to give the guest-free derivative **1**, which shows remarkable thermal stability in the temperature window 490–550 K. Above 550 K, **1** starts to decompose in two additional steps (Fig. S2†). Consequently, **1** was prepared by controlled thermal treatment of $1 \cdot PhNO_2$ at 480 K for 80 min in a N$_2$ stream. During this process, the crystals

deteriorated, thereby preventing us to analyse the structure through single crystal X-ray analysis. However, combination of magnetic and calorimetric measurements together with elemental analysis and room temperature powder X-ray diffraction (PXRD) analysis, show that essentially the framework structure of $1 \cdot PhNO_2$ is retained in 1 (*vide infra*) (see ESI†).

Spin crossover behaviour

The thermal dependence of the magnetic properties measured at 1 K min^{-1} and expressed as the product $\chi_M T$, where χ_M is the molar magnetic susceptibility and T is the temperature, is displayed in Fig. 1 (left) for $1 \cdot PhNO_2$. The $\chi_M T$ value equal to 3.79 cm^3 K mol^{-1} is consistent with a fully populated Fe^{II}–HS state in the range 300–280 K, which corresponds to $\gamma_{HS} = 1$ (state 1: HS). Below 280 K, $\chi_M T$ decreases in two overlapped steps, a first one gradual followed by a second steeper separated by a narrow inflexion at about 240–245 K with $\chi_M T \approx 2.55$ cm^3 K mol^{-1} that corresponds *ca.* $\gamma_{HS} \approx 2/3$ (state 2: HS$_{0.66}$LS$_{0.33}$). Then follows a plateau *ca.* 20 K wide centred at 225 K characterized by a $\chi_M T$ value 2.05 cm^3 K mol^{-1} and $\gamma_{HS} = 1/2$ (state 3: HS$_{0.5}$LS$_{0.5}$). This value, slightly higher than expected for the half of 3.79 cm^3 K mol^{-1}, may be the result of an increase of the orbital contribution of the Fe^{II} centre remaining HS in state 3. Upon cooling below 214 K, $\chi_M T$ drops again in a third step that leads to a new inclined plateau (206–199 K) with a value 1.30 cm^3 K mol^{-1} at 202 K (state 4: HS$_{0.33}$LS$_{0.66}$). Finally, below 199 K a sharp forth step leads the system to the completely populated LS state at 193 K ($\chi_M T \approx 0.1$ cm^3 K mol^{-1}) (state 5: LS). The heating and cooling modes of the $\chi_M T$ *vs.* T plot behaviour indicate the lack of any remarkable hysteresis.

The four steps were corroborated by differential scanning calorimetric (DSC) measurements carried out at 5 K min^{-1} (Fig. 1 left). The critical temperatures associated with the maxima/minima are 258, 236, 208 and 196 K. The associated average enthalpy variations, estimated from the area below each maximum, are $\Delta H_i \approx 7.60$, 3.36, 2.88 and 5.87 kJ mol^{-1}, respectively, and the corresponding average entropy variation being $\Delta S_i = \Delta H_i/T_{ci} = 29.45$, 14.24, 13.85 and 29.94 J K^{-1} mol^{-1}. These steps correspond well with the sequence of HS molar fraction $\gamma_{HS} = 1$ (state 1), $\gamma_{HS} \approx 2/3$ (state 2), $\gamma_{HS} = 1/2$ (state 3), $\gamma_{HS} \approx 1/3$ (state 4) and $\gamma_{HS} = 0$ (state 5) with overall ΔH_T and ΔS_T values are 19.8 kJ mol^{-1} and 87.48 J K^{-1} mol^{-1}. The entropy change does not correspond exactly to the ratio of spin conversion during the steps, which indicates that other phenomena like structural order may be involved in the transitions.

Photo-generation of the fully populated metastable HS* state (state 6), the so-called light induced excited spin state trapping (LIESST) experiment,[21] was carried out at 10 K irradiating a microcrystalline sample of $1 \cdot PhNO_2$ with green light ($\lambda = 532$ nm) (Fig. S4†). In these conditions, the sample saturates in 4 h, with values of $\chi_M T$ around 3.45 cm^3 K mol^{-1}. Subsequently, the light irradiation was switched off and the temperature increased at a rate of 0.3 K min^{-1}. Then, $\chi_M T$ slightly raises to a value of 3.58 cm^3 K mol^{-1} at 16 K, which practically corresponds to 95% of the maximum value obtained at 300 K. This
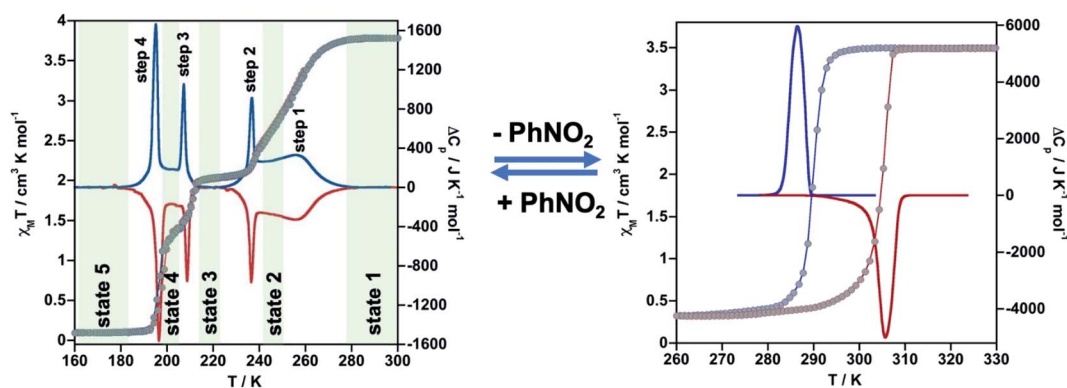

Fig. 1 Thermal dependence of magnetic (grey circles) and calorimetric properties of $1 \cdot PhNO_2$ (left) and 1 (right). Blue and red curves correspond to the cooling and heating modes in ΔC_p.

Table 1 Average bond lengths (Å), $\sum$ (deg) parameter, HS molar fraction γ_{HS} and spin states of $1 \cdot PhNO_2$

|	290 K	250 K	228 K	206 K	140 K	15 K	Photo 15 K
$\langle Fe-N_{ax} \rangle$	2.231(4)	2.158(5)	2.026(5) (LS), 2.219(5) (HS)	2.068(6)	2.015(4)	2.010(7)	2.203(6)
$\langle Fe-N_{eq} \rangle$	2.133 (4)	2.070(3)	1.944(2) (LS), 2.126(2) (HS)	1.996(4)	1.933(2)	1.932(3)	2.120(3)
$\langle Fe-N \rangle$	2.166(3)	2.099(2)	1.971(2) (LS), 2.157(2) (HS)	2.020(3)	1.960(2)	1.958(3)	2.147(3)
$\sum$	3.68(16)	3.40(16)	6.66(16) (LS), 5.40(17) (HS)	3.76(10)	4.40(15)	3.2(2)	4.72(18)
γ_{HS}	1	2/3	1/2	1/3	0	0	1
State	1 (HS)	2 (HSHSLS)^a	3 (HSLS)	4 (LSLSHS)^a	5 (LS)	5 (LS)	6 photo(HS)

^{a} Spin-state ordering not definitely characterized.
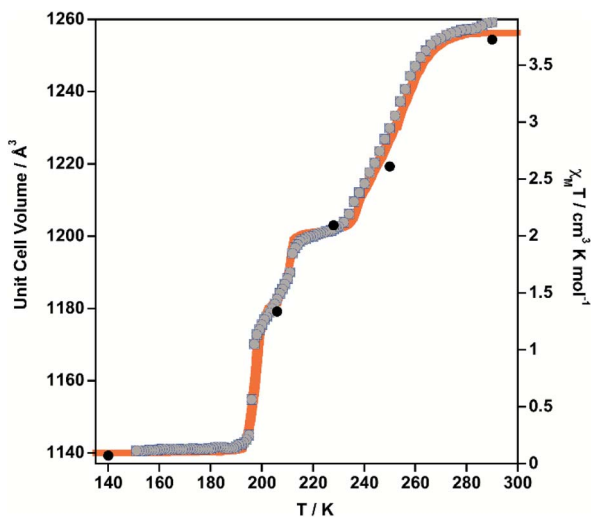
Fig. 2 Comparison of the thermal dependence of $\chi_M T$ (orange) and unit cell volume (grey dots) for **1·PhNO$_2$**. Black filled circles represent the volume–temperature coordinates at which the crystal structure has been solved (15 K LS and HS* data not shown).

raise in $\chi_M T$ as well as its value at 16 K reflect the thermal population of different microstates originated from the zero-field splitting of the HS* spin state. At higher temperatures, $\chi_M T$ decreases rapidly until joining the thermal SCO curve at *ca.* 55 K, indicating that the metastable HS* state has relaxed to the stable LS state. The relaxation is characterized by two distinct slopes with characteristic T_{LIESST} temperatures,[22] 30.0 K and 48 K, respectively, obtained from $\partial \chi_M T / \partial T$. The low T_{LIESST} temperatures are consistent with the relatively high critical SCO temperatures of **1·PhNO$_2$** and according to the inverse-energy-gap law.[23]

As mentioned above, controlled thermal desorption of PhNO$_2$ in **1·PhNO$_2$** affords the guest free species **1**. Upon desorption, the magnetic properties of **1** correspond to a complete single step spin transition characterized by a square-shaped thermal hysteresis 15 K wide (1 K min^{-1}) centred at room temperature with critical temperatures $T_c^{down} = 290.0$ K

and $T_c^{up} = 305.3$ K, which are consistent with those obtained from DSC measurements, 287.0 K and 305.6 K, respectively (Fig. 1 right). The average ΔH and ΔS values are 21.7 kJ mol^{-1} and 74.1 J K^{-1} mol^{-1}, respectively. These thermodynamic values for **1** from $\gamma_{HS} = 1$ to $\gamma_{HS} = 0$ differ from the sum of the values for **1·PhNO$_2$** over the different steps and confirm that the spin state switching is not the only process coming into play. Interestingly, the original multi-step SCO properties of the as-synthesized derivative **1·PhNO$_2$** are completely recovered when crystals of **1** are soaked in PhNO$_2$ for a week (Fig. S3†). This fact, together with the strong cooperative hysteretic behaviour, are clear proofs confirming the retention of the double interpenetrated porous structure in the desorbed material **1**.

Structure

Structure of 1·PhNO$_2$. X-ray single crystal studies were carried out for **1·PhNO$_2$**. The thermal dependence of the unit cell parameters was investigated to check its consistency with the magnetic measurements. The unit cell volume, *V*, and the $\chi_M T$ product virtually display the same multi-step SCO behaviour (Fig. 2), which is also mirrored by the remaining unit cell parameters *a*, *b*, *c* (see also Fig. S5†). Consequently, the crystal structure was analysed at 290, 250, 228, 206, 140 K, 15 K and at 15 K after laser irradiation, which correspond reasonably well with states 1, 2, 3, 4, 5 and 6, respectively. Relevant crystallographic data are collected in Table S1.† The average axial, equatorial and [Fe^{II}N$_6$] Fe–N bond lengths ($\langle$Fe–N$\rangle$) and average angular distortion Σ° [sum of the deviations from the ideal octahedron of the 12 "*cis*" N–Fe–N angles ($\Sigma^\circ = \Sigma_i |\theta_i - 90^\circ|$)] for all investigated temperatures are gathered in Table 1.

The structures found at 290 K (state 1, $\gamma_{HS} = 1$), 140 K, 15 K (state 5, $\gamma_{HS} \approx 0$) and 15 K after laser irradiation (state 6, $\gamma_{HS} \approx 1$) are isostructural and correspond to the monoclinic *P*2/*n* space group ($Z = 2$ ($Z' = 1$)) with similar unit cell parameters. In these unit cells, the two Fe sites lie on Wyckoff position with site symmetry 2 and are equivalent by symmetry (*n* glide plane). The main different features are the changes of Fe–N bond lengths, N–Fe–N angle and unit cell contraction, due to the molecular
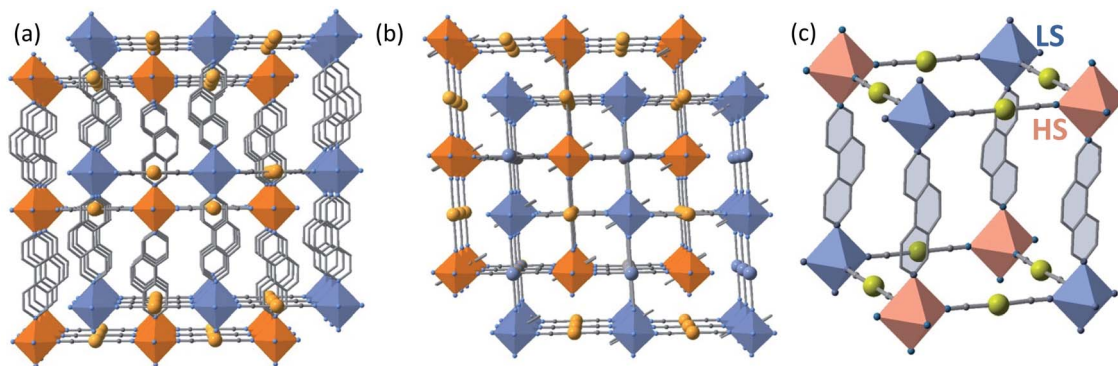

Fig. 3 View of the two interpenetrated frameworks (blue/orange) along [001] (a) and [010] (b) directions. (c) Fragment of one of the two frameworks in the state 3 ($\gamma_{HS} = 1/2$, 228 K) showing the LS (blue) and HS (pink) octahedral centers. Disorder in the central ring of 3,8-phen has been omitted for clarity.

volume change between LS and HS states. As expected, the linear 3,8-phen and $[Au(CN)_2]^-$ bridging ligands occupy, respectively, the axial and equatorial positions of the elongated $[Fe^{II}N_6]$ octahedral coordination site, thereby defining two identical and mutually interpenetrated 3D porous networks with pcu-type topology made up of $\{Fe[Au(CN)_2]_2\}_n$ layers pillared by 3,8-phen ligands (Fig. 3a and b). The structures are characterised by positional disorder of the central ring of the 3,8-phen ligand imposed by symmetry (see Fig. S6†). The variation of $\langle Fe-N \rangle$ between the 1(HS) and 5 (LS) states, $\Delta(\langle Fe-N \rangle)_{1-5} \approx 0.21$ Å is consistent with a complete SCO between the LS and the HS states of Fe^{II}. However, the value $\Delta(\langle Fe-N \rangle)_{6-5} \approx 0.19$ Å between 5(LS) and 6(HS*) at 15 K is 10% smaller but consistent with an almost complete spin-state conversion.

At 228 K (state 3), the crystal undergoes a symmetry breaking with a change of lattice periodicity from the monoclinic $P2/n$ space group to the monoclinic $I2/a$ ($Z = 8$ ($Z' = 2$)). Therefore, there are now 2 symmetry inequivalent Fe^{II} sites in the unit cell, remaining on the 2-fold axis: 4 Fe^{II} sites are LS as characterized by $\langle Fe-N \rangle_{LS} = 1.971(2)$ and the other 4 Fe^{II} sites are HS as characterized by $\langle Fe-N \rangle_{HS} = 2.157(2)$ Å. The average $\langle Fe-N \rangle_{LS+HS}$ equal to 2.064 Å is ca. 0.1 Å smaller than $\langle Fe-N \rangle = 2.166$ Å at 290 K thus corroborating that $\gamma_{HS} = 1/2$. This state 3 defines a long-range periodic $\cdots$LS–HS$\cdots$ ordering in both interpenetrated

frameworks. The HS and the LS sites alternate along the 3,8-phen and $[Au(CN)_2]^-$ groups as shown in Fig. 3c.

The two interpenetrated pcu-type frameworks interact with each other through strong aurophillic interactions leading to a characteristic 90° criss-cross pattern between the corresponding NC–Au–CN groups. The $Au\cdots Au$ distance gradually shortens at lower temperatures due essentially to the spin state change, being 3.0733(4) Å at 290 K and 2.9963(4) Å at 140 K. Interestingly, despite the interpenetration of the two frameworks, channels are formed along $a + c$ direction where the $PhNO_2$ molecules are located (Fig. 4a and b). Within the channels, the disordered $PhNO_2$ molecules are interposed between the two frameworks interacting with the 3,8-phen bridging ligands via π-stacking (Fig. 4b). The number of $C_{(3,8-phen)}\cdots C_{(PhNO_2)}$ contacts shorter than the sum of the van der Waals radii (ca. 3.70 Å) remains almost constant in number but they shorten as the LS state population increases (γ_{HS} decreases) at low temperatures, being in the range 3.39–3.69 Å (Fig. 4c). Furthermore, below 290 K a second type of short $C\cdots C$ contacts appear involving $PhNO_2$ molecules and the $[Au(CN)_2]^-$ bridges ($C_{(Au(CN)_2)}\cdots C_{(PhNO_2)} \approx 3.54$–3.68 Å) and weaken at 290 K ($C_{(Au(CN)_2)}\cdots C_{(PhNO_2)} > 3.70$ Å) (Fig. 4c).

Another relevant observation concerns the pseudo-square $\{Fe_4[Au(CN)_2]_4\}$ windows. They experience a scissor-like movement changing the acute Au–Fe–Au angle from 88.14° to 84.39°
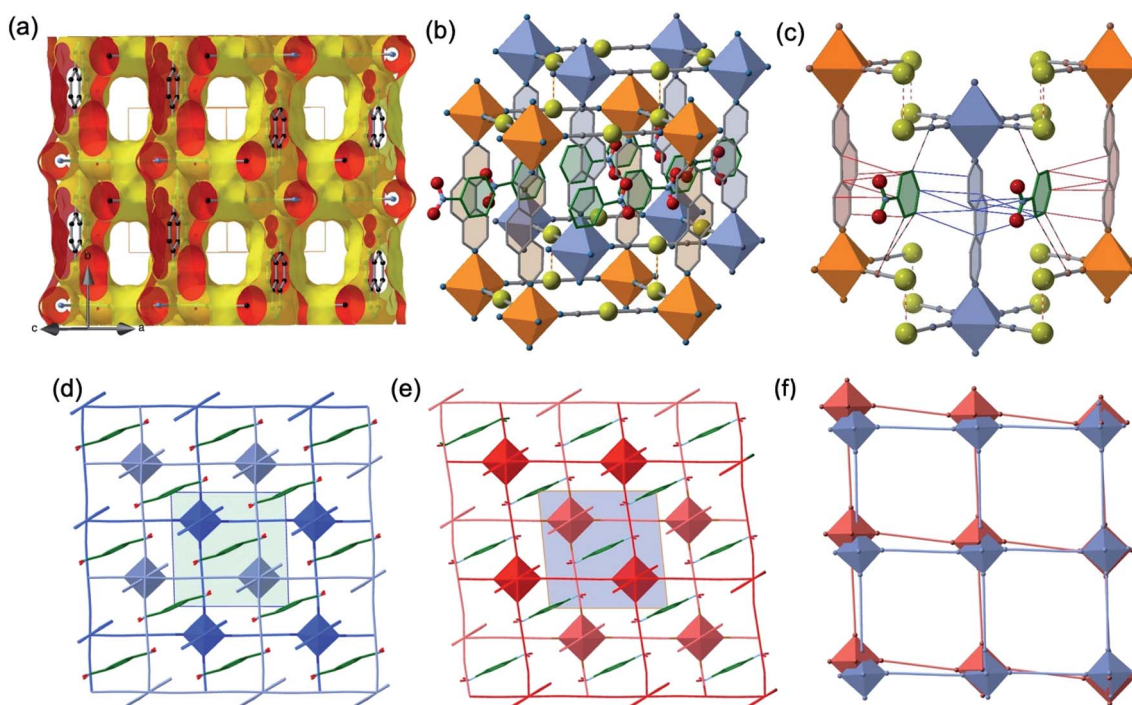

Fig. 4 (Top) View of a fragment of the interpenetrated pcu frameworks illustrating: (a) the solvent-excluded surface showing void channels running along $a + c$ direction; (b) the 1·PhNO₂ molecules located in the channels (the shown PhNO₂ molecule represents the average of two slightly disordered positions); and (c) $C_{(3,8-phen)}\cdots C_{(PhNO_2)}$ (red, blue thin bonds) and $C_{(Au(CN)_2)}\cdots C_{(PhNO_2)}$ (black-red thin bonds) intermolecular interactions shorter than the sum of van der Waals radii at 228 K. Red-white thin bonds correspond to the $Au\cdots Au$ interactions between the two interpenetrated frameworks. (Bottom) View down to [010] direction of the interpenetrated frameworks marked in light- and dark-blue LS state (d), light- and dark-red (HS state) (e) including the PhNO₂ molecule located in the channels (the inner green/blue squares correspond to the unit cell); (f) superposition of one of the two frameworks illustrating the distortion of the structure when moving from the LS state (blue) to the HS state (orange).
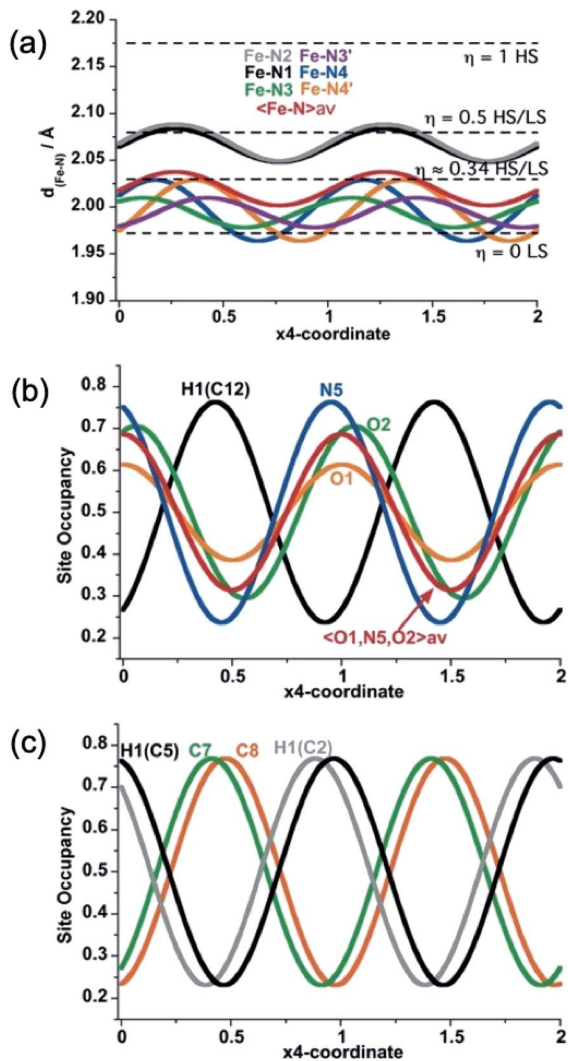
Fig. 5 Structural modulation at 206 K of the Fe−N bond lengths (a), the NO-site occupancy of the PhNO₂ guest molecule (b), and C7 and C8 atom sites along the two-fold axis of 3,8-phen ligand (H-atom modulations are included for comparison) (c).

($\Delta\phi = 3.75°$) when moving from the LS state 5 to the HS state 1 (see Fig. 4d–f).

As far as state 2 (250 K) and state 4 (206 K) are concerned, the structure does not change significantly, however, the average 3D space group $P2/n$ has a symmetry different from states 1, 3 and 5 because data shows an aperiodic feature denoted by the presence of satellite diffraction peaks at q-vector $\approx$ [0.433(5), 0.502(6), 0.359(5)] and [0.433(2), 0.498(2), 0.3689(18)] for state 2 and 4, respectively (see Fig. S7†). The satellite peaks provide evidence of aperiodic order but, unfortunately, we could not solve the structure with superspace approach for state 2 due to the weak signal/noise ratio of the satellites, and we only provide the average 3D periodic structure, where we found $\langle$Fe–N$\rangle$ = 2.099(5) Å, which agrees well with $\gamma_{HS} \approx 2/3$. In contrast, for state 4, the structural refinement in the $(3 + 1)$-dimensional superspace group $P2/n$ (a1|2g)0s ($Z = 2$ ($Z' = 1$)), indicates a spatial modulation of the Fe–N bond lengths (see Fig. 5),

which is aperiodic with the (a, b, c) lattice and $\langle$Fe–N$\rangle$=2.020(3) Å providing evidence for an aperiodic modulation of the HS fraction around $\gamma_{HS} \approx 1/3$ coupled to the structural reorganization. There is no group–subgroup relationship between states 2 and 3 and between states 3 and 4, consequently, both phase transitions are of first-order nature as shown in Fig. 1. The structure of state 4 is therefore no longer 3D periodic, but incommensurately modulated with respect to the initial (a, b, c) lattice, as it is the case for $\{Fe[(Hg(SCN)_3)_2](4,4'-bipy)_2\}_n$ and $[FeH_2L^{2-Me}][SbF_6]_2$, where spin state concentration waves also form.[24,25]

In summary, state 4 (and very likely state 2) corresponds to a long-range aperiodic order close to LS–LS–HS (HS–HS–LS), characterized by the modulation of the Fe–N bonds (Fig. 5a). This modulation also involves modulation of the guest PhNO₂ (Fig. 5b) and of the ligand (Fig. 5c). Since some satellite peaks are also observed in the LS state 5 at 140 K, the spatial modulation of HS/LS states is rather driven by the aperiodic ligand/solvent order. Therefore, the steps in γ_{HS} during the spin conversion are driven by a subtle balance between the spin crossover centres, ligand order and HS/LS order all influenced by the guest molecule.

Structure of 1. As mentioned above, **1** was prepared through careful thermal treatment from **1·PhNO₂**, under N₂ atmosphere. The desorption was monitored from room temperature until 480 K where the weight loss corresponded to *ca.* 97% of the guest molecule, then the sample was kept at this temperature for 80 min before cooling back to room temperature. Fig. 6 displays the PXRD pattern calculated for **1·PhNO₂** calculated from the single crystal data at 290 K and the experimental diffraction patterns of the microcrystalline powder, measured at room temperature both before and after desorbing the PhNO₂ molecule. At a glance, there are obvious drastic changes in the pattern when moving from **1·PhNO₂** to **1** due to the lack of guest molecules in the framework. Despite this, the peak centred at $2\theta \approx 7.7°$ ($d \approx 11.5$ Å), associated with the (0, 1, 0) reflection in **1·PhNO₂**, corresponds to the separation between two consecutive $\{Fe_4[Au(CN)_2]_4\}_n$ layers and is essentially retained in **1**. Rietveld refinement of the experimental data for **1** gives
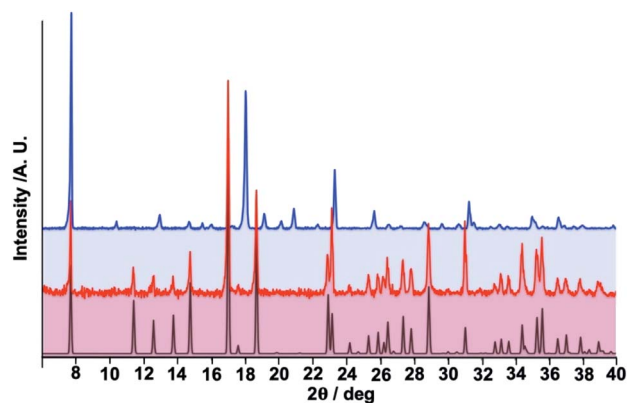

Fig. 6 Comparison of calculated and experimental (black and red lines) powder X-ray diffraction (PXRD) patterns for **1·PhNO₂** with the experimental PXRD of **1** (blue line).

a reasonable good fit for a possible slightly changed unit cell with crystal parameters $a = 12.0682(4)$ Å, $b = 16.9687(4)$ Å, $c = 11.4632(3)$ Å and $\beta = 94.888(4)°$, $Z = 4$. We found that several space groups, namely $C2/m$, $C2$, $P2_1/c$ and $P2/c$, are compatible with this unit cell and diffraction pattern. It is important to stress that the only difference between $1 \cdot PhNO_2$ and 1 stems from the distinct possible orientations of the axial bridging 3,8-phen ligand, which clearly reflects the increase of rotational freedom of the ligand 3,8-phen in the guest-free derivative. Therefore, we chose to carry out the refinement in the space group $C2/m$ that accounts for all the possible orientations of the 3,8-phen linker while maintaining the connectivity of the original structure described for $1 \cdot PhNO_2$. A rather good fit of the PXRD pattern is shown in Fig. S8† for the $C2/m$ space group. A selection of crystallographic data, bond lengths and angles are summarized in Tables S2 and S3,† while a graphical description of the structure is shown in Fig. S8–S11.†

Discussion

The four-step SCO behaviour is a rare event so far studied, at the best of our knowledge, in three different Fe^{II} Hofmann-type clathrates loaded with hydroxilic solvents (H_2O, EtOH and/or DMF) which are stabilised in the pores by host–guest and guest–guest hydrogen bonding interactions facilitated by the presence of acceptor/donor centres associated with the pillar ligands. For example, in the 2D system $\{Fe^{II}(saltrz)_2[M(CN)_4]\} \cdot 8/3H_2O$ (M = Pd, Pt) the trapped water molecules interact *via* hydrogen bonding with the phenyl and triazole groups of the terminal ligand saltrz thereby generating structural constraints leading to four-step SCO behaviour.[18] A similar situation has been described for the 3D systems $\{Fe^{II}(bipydz)[Au(CN)_2]_2\} \cdot 4EtOH$[19] and $\{Fe^{II}(4-abpt)[Ag(CN)_2]_2\} \cdot 2DMF \cdot EtOH$[20] where the pillar ligands bipydz and 4-abpt contain 1,2-diazine and aminotriazole moieties, respectively. For the $[Au(CN)_2]^-$ derivative of the latter compound a seven/eight step behaviour has been recently reported.[26]

Unlike these examples, compound $1 \cdot PhNO_2$ introduces two new relevant features. First, the low dielectric environment of the channels, defined by the aromatic rings of the 3,8-phen ligands, capable of discriminating between hydroxylic solvents such as MeOH or H_2O and benzene derivatives like $PhNO_2$, which are easily recognised *via* π-stacking. Consequently, in the present system, host–guest π–π supramolecular interactions are the relevant promoters of four-step SCO. Second, the guest-free derivative 1 displays a strong cooperative SCO featuring a 20 K wide hysteresis centred at room temperature (290 K), which upon reversible adsorption of $PhNO_2$ regenerates $1 \cdot PhNO_2$ with identical four-step SCO behaviour. The complete single-step bistable SCO behaviour of the guest-free derivative 1 is consistent with that reported for the homologous coordination polymers of general formula $\{Fe^{II}(L)[Au(CN)_2]_2\}$ with L = pyrazine and 2-fluoropyrazine, which share: (i) the same $\{Fe^{II}_4[Au^I(CN)_2]_4\}_\infty$ grids connected through rigid axial linear ligands; and (ii) the lack of guest molecules interposed between the two interpenetrated 3D frameworks. These facts ensure efficient communication between the Fe^{II} centres in each

independent 3D framework favouring "ferro-like" elastic interactions due to the lack of significant local elastic frustration. In contrast, inclusion of $PhNO_2$ as a molecular "wedge" between the two 3D frameworks, introduces two types of host–guest interactions between the interpenetrated frameworks: (i) C···C short contacts with the $[Au(CN)_2]^-$ and (ii) π–π interactions with the 3,8-phen ligands. Clearly opposed to the contraction of the frameworks upon cooling, these interactions may act also as a source of intermolecular "friction" preventing the possible mutual sliding of the 3D frameworks. These facts not only deeply modify the elastic properties of the crystal introducing elastic frustration, clearly seen as a sequence of plateaus with locked fractions of γ_{HS} separating the steps,[5] but also manifested by an energy cost reflected on the destabilisation of the LS state.

The intermediate plateaus usually reflect ordered populations of HS and LS states, as expected for a succession of "antiferro-like" states.[24] Particular relevance has, in the present case, the relative large thermal stability of the state 3 at $\gamma_{HS} = 1/2$ where the unit cell doubles and the LS–HS Fe^{II} centres, connected through 3,8-phen and $[Au(CN)_2]^-$, alternate in the two interpenetrated frameworks (Fig. 3c). This thermal stability reflects the extra energy-cost associated with erasing the structural ordering observed in this phase. Indeed, this energy penalisation can be described in terms of structural modifications. The most relevant structural changes to remark are the ⟨Fe–N⟩ bond lengths and more importantly the large increase of the angular distortion parameter of the $[FeN_6]$ when moving to the state 3 (see Σ value Table 1), a fact which is correlated with the noticeable change of the scissor-like angles of the $\{Fe_4[Au(CN)_2]_4\}$ windows (see Fig. 4d–f). These changes do not impose any toll for 1 since the intermolecular "friction" between the frameworks is minimised. However, the steric hindrance introduced by $PhNO_2$ in $1 \cdot PhNO_2$ between them, reaches a maximum for state 3 ($\gamma_{HS} = 1/2$). This is clearly illustrated by the increase of the angular distortion (Σ) of the HS and LS Fe^{II} octahedrons by *ca.* 150% in state 3. Apparently, state 2 ($\gamma_{HS} \approx 2/3$) and state 4 ($\gamma_{HS} \approx 1/3$) can be considered less energy cost symmetric "replicas" paving the way for achieving the state $\gamma_{HS} = 1/2$, which can be considered the bottleneck of the HS ↔ LS conversion in $1 \cdot PhNO_2$. Detailed crystallographic analysis of state 4 sheds light for the generation of an aperiodic order of HS and LS states, which also could be inferred in a similar aperiodic modulation for state 2.

Conclusions

Here we have reported on a singular Fe^{II} Hofmann-type porous coordination polymer whose magnetic, optical and mechanical properties can be reversibly switched between two uncommon SCO behaviours, namely a room temperature single-step strong cooperative spin transition and four-step SCO behaviour. The key of the reversible switch between both behaviours is the absence or presence of a molecule of $PhNO_2$ in the 1D channels. The easy recognition of $PhNO_2$ *via* π-stacking through the aromatic walls of the 1D channels defined by the 3,8-ligands introduces a sort of "molecular wedge" mechanism between the

two interpenetrated 3D frameworks which provokes elastic frustration and multistep behaviour. It is worth noting that we have successfully extended these results to other six-membered aromatic guests such as fluoro-, chloro-, bromo- and 1,3-bibromo-benzene, benzaldehyde or benzonitrile among others. These preliminary results, which will be reported elsewhere, show that the new **1·PhX** clathrates display similar four-step SCO behaviour, thereby demonstrating the reliability of the dual system here reported.

Robust SCO compounds with wide hysteretic behaviour centred at room temperature such as **1**, are potentially interesting materials for the construction of sensor, micro/nano electronic and spintronic devices.

Experimental

$K[Au(CN)_2]$, and $Fe(BF_4)_2 \cdot 6H_2O$ were purchased from commercial sources and used as received whereas the synthesis of the 3,8-phen ligand was performed as described in a precedent work.[27]

Materials

Synthesis of 1·PhNO$_2$. As mentioned above, crystals of **1·PhNO$_2$** were grown by slow liquid–liquid diffusion technique using a modified H-vessel (total volume *ca.* 10 mL) with a third tube added due to the poor solubility of the 3,8-phen ligand in methanol. The peripheral tubes contained $Fe(BF_4)_2 \cdot 6H_2O$ (0.056 mmol, 19 mg) and $K[Au(CN)_2]$ (0.116 mmol, 33.5 mg) salts, respectively while the central tube contained 3,8-phen ligand (0.055 mmol, 10 mg). Each tube was partially filled first with a methanol and then with a solution 1 : 10 of PhNO$_2$ in methanol, finally the tubes were sealed. Yield *ca.* 50%. Calcd for $C_{22}H_{13}N_7O_2FeAu_2$: C, 30.83; H, 1.53; N, 11.44. Found: C, 31.12; H, 1.59; N, 11.72. IR: $\nu(C\equiv N) = $ 2179.2 cm^{-1} (*vs.*), $\nu(NO_2)_{as} = $ 1523 cm^{-1} (*vs.*) and $\nu(NO_2)_{sym} = $ 1343 cm^{-1} (*vs.*). The guest-free derivative **1** was obtained by controlled thermal decomposition under Ar atmosphere. Calcd for $C_{16}H_8N_6FeAu_2$: C, 26.18; H, 1.10; N, 11.45. Found: C, 26.63; H, 1.16; N, 11.51. This chemical analysis could reflect a residual amount of PhNO$_2$ in the range of *ca.* 3–4% remaining in the structure, indeed the IR spectrum clearly denoted the lack of significant $\nu(NO_2)_{as}$ and $\nu(NO_2)_{sym}$ vibrational modes.

Physical characterisation

Magnetic measurements. Variable-temperature magnetic susceptibility data for bulk crystalline/microcrystalline samples **1·PhNO$_2$** and **1** (*ca.* 20 mg) were recorded with a Quantum Design MPMS2 SQUID susceptometer equipped with a 7 T magnet, operating at 1 T and at temperatures 10–400 K. Experimental susceptibilities were corrected for diamagnetism of the constituent atoms by the use of Pascal's constants. The LIESST experiments were performed at 10 K in a commercial sample holder (Quantum Design Fiber Optic Sample Holder), wherein a quartz bucket containing 1.20 mg of crystals of **1·PhNO$_2$**, was held against the end of a quartz fiber coupled with a green laser (532 nm). The raw data was corrected for a background arising from the sample holder. The resulting magnetic signal was calibrated by scaling to match obtained high temperature values with those of bulk sample.

Calorimetric and thermogravimetric measurements. Differential scanning calorimetry measurements were performed using a Mettler Toledo DSC 821e calorimeter. Low temperatures were obtained with an aluminium block attached to the sample holder, refrigerated with a flow of liquid nitrogen and stabilized at a temperature of 110 K. The sample holder was kept in a dry box under a flow of dry nitrogen gas to avoid water condensation. The measurements were carried out using around 12 mg of microcrystalline **1·PhNO$_2$** or **1** sealed in aluminium pans with a mechanical crimp. Temperature and heat flow calibrations were made with standard samples of indium by using its melting transition (429.6 K, 28.45 J g^{-1}). An overall accuracy of ±0.2 K in temperature and ±2% in the heat capacity is estimated. The uncertainty increases for the determination of the anomalous enthalpy and entropy due to the subtraction of an unknown baseline.

Thermogravimetric analysis was performed on a Mettler Toledo TGA/SDTA 851e, in the 290–800 K temperature range under a nitrogen atmosphere with a rate of 10 K min^{-1}.

Powder X-ray diffraction measurements (PXRD). PXRD measurements where performed on a PANalytical Empyrean X-ray powder diffractometer (Cu K$_\alpha$ radiation) equipped with a PIXcel detector operating at 40 mA and 45 kV. PXRD data for **1** for Rietveld refinement was collected in the 5–90° (2θ) angular range with a step size of 0.013° and using a 0.5 mm glass capillary and soller slits of 0.02° and a divergence slit of 1/4°. DICVOL06 was used to determine the cell parameters by indexing the PXRD pattern of **1**. This yielded a monoclinic unit cell with $a = 12.063$ Å, $b = 16.960$ Å, $c = 11.457$ Å, $\beta = 94.9°$, which was further refined against the experimental PXRD in the $C2/m$ space group by the LeBail method using the FULLPROF software package. These results were used to build a structural model of **1** with Materials Studio (MS) 2017 based on the original structure of **1·PhNO$_2$**, solved by SCXR measurements. This model was used as a starting point for a Rietveld refinement, which was carried out with TOPAS Academic 5 program (http://www.topas-academic.net/).

Single crystal X-ray diffraction. Single-crystal X-ray diffraction data for $\{Fe^{II}(3,8phen)[Au(CN)_2]_2\} \cdot PhNO_2$ at 250 K, 228 K, 206 K and 140 K were collected on the same single crystal. The temperature series has been completed with data at 290 K on a second crystal. A new single crystal was also selected for data taken at 15 K and at 15 K, without and under light exposure with a green laser ($\lambda = 532$ nm at 3 mW for 2 h, this includes duration of data collection). Additionally, the temperature variation of the unit cell parameters within 290 K to 140 K range both in cooling and heating mode with 2–3° intervals was measured on one crystal (the same as crystal structure data at 290 K data).

A Xcalibur 3 four-circle diffractometer (Oxford Diffraction) equipped with a 2D Sapphire3 CCD detector with Mo Kα radiation ($\lambda = 0.71073$ Å), was used for all data collection. An Oxford Cryosystems 700Plus nitrogen-flow cryostat was used for measurements in the temperatures ranging from 290 K down to 140 K; and an Oxford Diffraction Helijet helium-flow cryostat for measurements at 15 K.

The unit cell parameters and the data reduction were obtained with the CrysAlisPro (CrysAlisPro 1.171.38.41, Rigaku

OD, 2015) software from Oxford Diffraction. During data processing a data scaling and empirical or multi-scan absorption correction were also performed with CrysAlisPro software. The structures at 290 K, 250 K, 228 K, 140 K, 15 K and 15 K after laser irradiation, with the exception of 206 K data, were solved in $P2/n$ space group by direct methods using SHELXT[28] and refined by full-matrix least squares on F^2 using SHELXL,[29] see Table S1,† with Olex2 GUI.[30] All non-hydrogen atoms were refined anisotropically and H-atoms were constrained by geometry. When applicable, DFIX, SIMU and ISOR restraints as well EADP constraints were applied for occupational disorders. For 228 K a cell doubling has been identified; the satellites at Q-vector $\sim 0.5a* + 0.5b* + 0.5c*$ accompanied with a weak diffuse signal, were found and, since a β-angle is $\sim 90°$, a monoclinic $I2/a$ space group was assigned. Detailed analysis at 206 K revealed a presence of incommensurate satellite peaks with a q-vector $\sim 0.431(2)a* + 0.498(2)b* + 0.3690(18)c*$, Fig. S7.† These satellites start to appear already for 250 K data (a weak signal), are stronger at 206 K and tend to slowly diminish with temperature, still present at 140 K, and missing for 290 K and 15 K data. Refinement in (3 + 1)-dimensional superspace: $P2/n$(a1|2g)0s, has been performed only for 206 K data. Here, the average structure model was solved by charge flipping and used for further least square refinement on F with Jana2006.[31] The modulation of the atomic positions for all non-H atoms as well as the first harmonic modulation wave for selected atom sites were refined. All H-atoms were constrained by geometry. A final refinement cycle was stable and allowed refinement of the basic structure parameters along with modulation parameters for all non-H atoms with the exception of $PhNO_2$ site.

The crystal data collection and refinement parameters for all phases are given in Table S1.† CCDC-2010360 (state 1, 290 K), CCDC-2010361 (state 2, 250 K), CCDC-2010362 (state 3, 228 K), CCDC-2010363 (state 4, 206 K), CCDC-2010364 (state 5, 140 K), CCDC-2010365 (state 5, 15 K [dark]) and CCDC-2010366 (state 6, 15 K [532 nm]) contain the ESI crystallographic data for this paper.†

Conflicts of interest

There are no conflicts to declare.

Acknowledgements

Notes and references

1 (a) E. König, *Struct. Bonding*, 1991, **76**, 51–152; (b) P. Gütlich, A. Hauser and H. Spiering, *Angew. Chem., Int. Ed.*, 1994, **33**, 2024–2054; (c) J. A. Real, A. B. Gaspar, V. Niel and M. C. Muñoz, *Coord. Chem. Rev.*, 2003, **236**, 121–141; (d) P. Gütlich and G. Goodwin, *Top. Curr. Chem.*, 2004, 233–235; (e) J. A. Real, A. B. Gaspar and M. C. Muñoz, *Dalton Trans.*, 2005, 2062–2079; (f) M. A. Halcrow, *Polyhedron*, 2007, **26**, 3523–3576; (g) A. Bousseksou, G. Molnár, L. Salmon and W. Nicolazzi, *Chem. Soc. Rev.*, 2011, **40**, 3313–3335.

2 C. Enachescu, M. Nishino and S. Miyashita, in *Spin-Crossover Materials Properties and Applications*, ed. M. A. Halcrow, Wiley, 2013, pp. 455–474.

3 C. Enachecu and W. Nicolazzi, *C. R. Chim.*, 2018, **21**, 1179–1195.

4 H. Watanabe, K. Tanaka, N. Bréfuel, H. Cailleau, J.-F. Létard, S. Ravy, P. Fertey, M. Nishino, S. Miyashita and E. Collet, *Phys. Rev. B*, 2016, **93**, 014419.

5 M. Paez-Espejo, M. Sy and K. Boukheddaden, *J. Am. Chem. Soc.*, 2016, **138**, 3202–3210.

6 R. Traiche, M. Sy and K. Boukheddaden, *J. Phys. Chem. C*, 2018, **122**, 4083–4096.

7 (a) M. Cavallini, I. Bergenti, S. Milita, J. C. Kengne, D. Gentili, G. Ruani, I. Salitros, V. Meded and M. Ruben, *Langmuir*, 2011, **27**, 4076–4081; (b) P. N. Martinho, C. Rajnak and M. Ruben, in *Spin-Crossover Materials: Properties and Applications*, ed. M. A. Halcrow, Wiley, 2013, pp. 376–404; (c) G. Molnar, S. Rat, L. Salmon, W. Nicolazzi and A. Bousseksou, *Adv. Mater.*, 2018, **30**, 17003862.

8 (a) M. C. Muñoz and J. A. Real, *Coord. Chem. Rev.*, 2011, **255**, 2068–2093; (b) Z.-P. Ni, J.-L. Liu, Md. N. Hoque, W. Liu, J.-Y. Li, Y.-C. Chen and M. L. Tong, *Coord. Chem. Rev.*, 2017, **335**, 28–43.

9 V. Martínez, A. B. Gaspar, M. C. Muñoz, G. V. Bukin, G. Levchenko and J. A. Real, *Chem.–Eur. J.*, 2009, **15**, 10960–10971.

10 W. Liu, L. Wang, Y.-J. Su, Y.-C. Chen, J. Tucek, R. Zboril, Z.-P. Ni and M.-L. Tong, *Inorg. Chem.*, 2015, **54**, 8711–8716.

11 N. F. Sciortino, F. Ragon, K. A. Zenere, P. D. Southon, G. J. Halder, K. W. Chapman, L. Piñeiro-López, J. A. Real, C. J. Kepert and S. M. Neville, *Inorg. Chem.*, 2016, **55**, 10490–10498.

12 K. A. Zenere, P. W. Doheny, S. G. Duyker, E. Trzop, E. Collet, B. Chan, P. W. Doheny, C. J. Kepert and S. M. Neville, *Chem. Sci.*, 2018, **9**, 5623–5629.

13 (a) V. Niel, J. M. Martinez-Agudo, M. C. Muñoz, A. B. Gaspar and J. A. Real, *Inorg. Chem.*, 2001, **40**, 3838–3839; (b) S. Bonhommeau, G. Molnár, A. Galet, A. Zwick, J. A. Real, J. J. McGarvey and A. Bousseksou, *Angew. Chem., Int. Ed.*, 2005, **44**, 4069–4073; (c) M. Ohba, K. Yoneda, G. Agustí, M. C. Muñoz, A. B. Gaspar, J. A. Real, M. Yamasaki, H. Ando, Y. Nakao, S. Sakaki and S. Kitagawa, *Angew. Chem., Int. Ed.*, 2009, **48**, 4767–4771; (d) G. Agustí, R. Ohtani, K. Yoneda, A. B. Gaspar, M. Ohba, J. F. Sánchez-Royo, M. C. Muñoz, S. Kitagawa and J. A. Real, *Angew. Chem., Int. Ed.*, 2009, **48**, 8944–8947.

14 I. A. Gural'skiy, B. O. Golub, S. I. Shylin, V. Ksenofontov, H. J. Shepherd, P. R. Raithby, W. Tremel and I. O. Fritsky, *Eur. J. Inorg. Chem.*, 2016, 3191–3195.

15 F. J. Valverde-Muñoz, M. Seredyuk, M. C. Muñoz, K. Znovjyak, I. O. Fritsky and J. A. Real, *Inorg. Chem.*, 2016, **55**, 10654–10665.

16 N. F. Sciortino, K. R. Scherl-Gruenwald, G. Chastanet, G. J. Halder, K. W. Chapman, J.-F. Létard and C. J. Kepert, *Angew. Chem., Int. Ed.*, 2012, **51**, 10154–10158.

17 M. J. Murphy, K. A. Zenere, F. Ragon, P. D. Southon, C. J. Kepert and S. M. Neville, *J. Am. Chem. Soc.*, 2017, **139**, 1330–1335.

18 N. F. Sciortino, K. A. Zenere, M. E. Corrigan, G. J. Halder, G. Chastanet, J.-F. Létard, C. J. Kepert and S. M. Neville, *Chem. Sci.*, 2017, **8**, 701–707.

19 J. E. Clements, J. R. Price, S. M. Neville and C. J. Kepert, *Angew. Chem., Int. Ed.*, 2016, **55**, 15105–15109.

20 W. Liu, Y.-Y. Peng, S.-G. Wu, Y.-C. Chen, Md. N. Hoque, Z.-P. Ni, X.-M. Chen and M.-L. Tong, *Angew. Chem., Int. Ed.*, 2017, **56**, 14982–14986.

21 S. Decurtins, P. Gütlich, P. C. Köhler, H. Spiering and A. Hauser, *Chem. Phys. Lett.*, 1984, **105**, 1–4.

22 J. F. Létard, P. Guionneau, L. Rabardel, J. A. K. Howard, A. E. Goeta, D. Chasseau and O. Kahn, *Inorg. Chem.*, 1998, **87**, 4432–4441.

23 (*a*) A. Hauser, *Coord. Chem. Rev.*, 1991, **111**, 275–290; (*b*) A. Hauser, C. Enachescu, M. L. Daku, A. Vargas and N. Amstuz, *Coord. Chem. Rev.*, 2006, **250**, 1642–1652.

24 E. Trzop, D. Zhang, L. Piñeiro-Lopez, F. J. Valverde-Muñoz, M. C. Muñoz, L. Palatinus, L. Guerin, H. Cailleau, J. A. Real and E. Collet, *Angew. Chem., Int. Ed.*, 2016, **55**, 8675–8679.

25 E. Collet, H. Watanabe, N. Bréfuel, L. Palatinus, L. Roudaut, L. Toupet, K. Tanaka, J.-P. Tuchagues, P. Fertey, S. Ravy, B. Toudic and H. Cailleau, *Phys. Rev. Lett.*, 2012, **109**, 257206.

26 Y. Y. Peng, S. G. Wu, Y. C. Chen, W. Liu, G. Z. Huang, Z. P. Ni and M. L. Tong, *Inorg. Chem. Front.*, 2020, **7**, 1685–1690.

27 E. Botana, E. Da Silva, J. Benet-Buchholz, P. Ballester and J. de Mendoza, *Angew. Chem., Int. Ed.*, 2007, **46**, 198–201.

28 G. M. Sheldrick, *Acta Crystallogr., Sect. A: Found. Adv.*, 2015, **71**, 3–8.

29 G. M. Sheldrick, *Acta Crystallogr., Sect. C: Struct. Chem.*, 2015, **71**, 3–8.

30 O. M. Dolomanov, L. J. Bourhis, R. J. Gildea, J. A. K. Howard and H. Puschmann, *J. Appl. Crystallogr.*, 2009, **42**, 339–341.

31 V. Petricek, M. Dusek, and L. Palatinus. *JANA2006*, Institute of Physics, Praha, Czech Republic.